Article

Bud-Neck Scaffolding as a Possible Driving Force in ESCRT-Induced Membrane Budding

Moritz Mercker[1,*] and Anna Marciniak-Czochra[1]
[1]Institute of Applied Mathematics, BioQuant and IWR, University of Heidelberg, Heidelberg, Germany

ABSTRACT Membrane budding is essential for processes such as protein sorting and transport. Recent experimental results with ESCRT proteins reveal a novel budding mechanism, with proteins emerging in bud necks but separated from the entire bud surface. Using an elastic model, we show that ESCRT protein shapes are sufficient to spontaneously create experimentally observed structures, with protein-membrane interactions leading to protein scaffolds in bud-neck regions. Furthermore, the model reproduces experimentally observed budding directions and bud sizes. Finally, our results reveal that membrane-mediated sorting has the capability of creating structures more complicated than previously assumed.

INTRODUCTION

Protein-induced membrane budding is fundamental for many normal and pathogenic biological processes (1). Well studied mechanisms are typically driven by proteins coating the entire bud surface, such as clathrin and COPI/II (2). However, recent experiments have revealed a different budding mechanism wherein protein complexes belonging to the endosomal sorting complex required for transport (ESCRT) spontaneously induce membrane budding and are predominantly localized in the neck region of these buds (3). In vivo, the ESCRT machinery plays a key role in lysosomal protein degradation. It mediates the invagination and scission of intralumenal vesicles, as well as the selective transport of ubiquitinated cargo into them, the final processes constituting the biogenesis of multivesicular bodies (MVBs) from early endosomes (4). ESCRTs are also involved in other cellular processes, including budding of most enveloped viruses (5–7).

During recent years, striking progress has been made in the functional and structural understanding of the ESCRT family, which mainly consists of the ESCRT-0, ESCRT-I, ESCRT-II, and ESCRT-III complexes (5,6). In a minimal setup, ESCRT-0 appears to arrange cargo clustering, ESCRT-I/II induces membrane buds (where addition of the ESCRT-III subunit Vps20 enforces the ESCRT-I/II bud-neck localization), and ESCRT-III leads to vesicle scission (3,8). In addition, diverse structural data provide insights into the composition and shape of these complexes, including interaction sites for mutual, lipid, and ubiquitin binding (1,6,9). In this study, we focus on the budding process, and hence we use ESCRT as a synonym for the protein supercomplex consisting of ESCRT-I, ESCRT-II, and Vps20.

Despite this detailed structural and functional knowledge, little is known about the mechanism of ESCRT-induced budding. Most existing models are incomplete and speculative, since they do not consider the underlying physics. They assume one of the following mechanisms: 1) asymmetric bilayer insertion, 2) modification and use of local lipid composition, or 3) intrinsic protein curvature forcing of membrane bending (scaffolding) (10–12). Indeed, there exists experimental evidence that all three mechanisms could be involved in ESCRT-induced budding.

First, it has been proposed that different subunits of ESCRT proteins include regions capable of membrane insertion. For example, the Vps37 subunit of ESCRT-I and the Vps22 subunit of ESCRT-II may insert via cationic helices at their N-termini, whereas the ESCRT-III subunit Vps20 appears to interact with a myristoylated N-terminus (13–16). Interestingly, there is evidence that insertion of cationic, amphipathic helices into membranes induces negative Gaussian curvature (17–19), which is the typical curvature associated with bud necks (20).

Second, it is hypothesized that ESCRTs induce lipid cluster formation, with the main shaping force provided by the line tension at lipid domain boundaries (20). Indeed, recent results show ESCRT-II-induced lateral lipid phase separation (21), and theoretical calculations give realistic equilibrium shapes for sufficiently high line tensions (20). However, related real line tensions seem to be not large enough to drive ESCRT-induced budding alone (21). Furthermore, the experimentally observed inward budding direction cannot be explained using these models, since budding opposed to the initial vesicle curvature appears to be energetically unfavorable.

Submitted August 6, 2014, and accepted for publication December 23, 2014.

*Correspondence: mmercker_bioscience@gmx.de

This is an open access article under the CC BY-NC-ND license (http://creativecommons.org/licenses/by-nc-nd/4.0/).

Editor: Tobias Baumgart.

© 2015 The Authors

0006-3495/15/02/0833/11 $2.00

http://dx.doi.org/10.1016/j.bpj.2014.12.040

Third, the possibility of scaffolding due to ESCRTs has been considered, since these proteins show typical features, such as high intrinsic (partially crescent-shaped) protein curvatures and strong membrane interactions, as well as sensing and induction of strong membrane curvatures (8,9,17,22,23). Furthermore, ESCRT-I/II structurally fits into the bud neck, leading to the schematic spokes model, according to which six to eight copies of ESCRT-I/II dock in the bud neck (9) (Figs. 1 and 2 *c*). However, the question of how ESCRT shapes might create budded structures remains open, since the process includes a complex interplay between protein shape and membrane curvature.

In this study, we assume that ESCRT-I/II complexes locally induce a negative Gaussian curvature within the membrane, and we deduce model parameters from experimentally observed protein shapes. In summary, such induction of negative Gaussian curvature is supported by 1) structural data suggesting that the ESCRT-I/II shape fits the bud neck (9); 2) the existence of cationic helices in ESCRT-I/II, which have been predicted to induce negative Gaussian curvatures (17–19); and 3) the high structural flexibility of ESCRT-I/II, a property that also has been linked to the induction of negative Gaussian curvature (19).

Moreover, it has been recently shown that the Influenza virus M2 protein actively generates negative Gaussian curvatures within membranes (24). This protein is strongly related to ESCRTs in the sense that in other viruses (such as HIV and Ebola) ESCRTs are assumed to undertake the function of M2 during viral membrane budding (24).

An alternative mechanism leading to experimentally observed patterns may include a form of Turing-type patterning. However, as discussed in the Supporting Material, most assumptions for these alternative models are not supported by experimental ESCRT data.

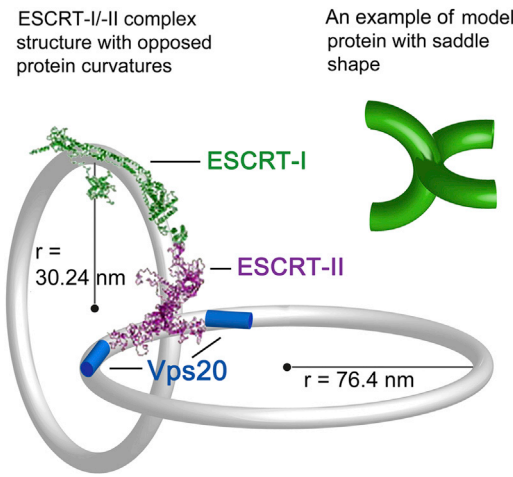

FIGURE 1 Illustration of model protein shapes deduced from structural protein data. The ESCRT-I/II + Vps20 complex is composed of two elongated elements with opposing curvatures. Thus, simulated model proteins (*light green*) are saddle-shaped. (ESCRT protein structure is modified from Boura et al. (9)). To see this figure in color, go online.

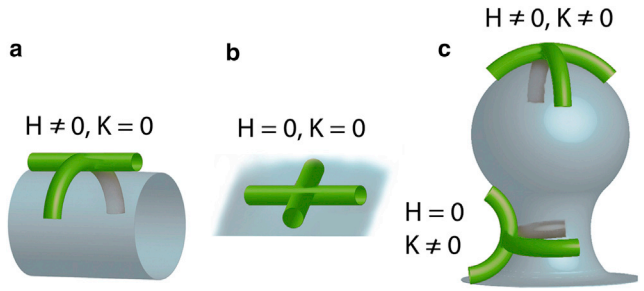

FIGURE 2 Protein shapes related to common membrane geometries. Shown are tube (*a*), flat-membrane (*b*), and budded-vesicle (*c*) geometries, as well as the corresponding local mean (*H*) and Gaussian curvatures (*K*). In the case of a saddle shape (*c*), the local geometry is described via a negative Gaussian curvature, since the mean curvature vanishes. To see this figure in color, go online.

Experimental and theoretical studies of dynamics of protein-membrane interactions are subject to strong limitations (25). Since the relevant scales are below the capability of observation of microscopic details, molecular dynamics (MD) methods have been developed as a powerful tool for simulating membrane-protein interactions at the molecular level (26,27). Although the general drawback of these methods is the high computational cost of simulating large systems, the accessible time- and spacescales continue to increase, making these techniques increasingly attractive even for relatively large systems (see examples in the literature (28–30)).

An alternative approach to the investigation of membrane behavior is being offered by continuum-based models in the framework of elasticity theory (31). It is based on the minimization of membrane free energy, leading to nonlinear partial differential equations. In contrast to the MD approaches, continuous models do not explicitly consider molecular interactions but incorporate energetic and entropic effects in a less detailed manner. Therefore, the computational effort depends on the required resolution in time and space, not on the simulated scales. Such models account for mechanochemical molecule properties, such as shape and stiffness, in the terms of macroscopic elastic parameters. They have proven to reproduce and explain a range of experimental membrane patterns (31,32). The continuous approach, previously restricted to the analysis of equilibrium configurations, has been recently extended to dynamical membrane processes (33).

MATERIALS AND METHODS

Model and simulation

In this section, we develop a continuous model to investigate the interplay between ESCRT protein shapes and membrane dynamics. The model is based on passive gradient flows of free energy, consistent with the experimental observation that ESCRT induces membrane budding without consuming energy (3). Dynamic model equations are given in terms of a nonlinear partial differential equation (PDE) system of fourth order related to the Willmore flow and to the Cahn-Hilliard equation. The

free energy used here is a generalization of the well known Helfrich energy for membranes (34). Detailed information about the modeling approach and the computation scheme can be found in our previous work (33). Novel aspects of the more general form of free energy used here are explained in the following section, as well as in the Supporting Material, including Fig. S2.

Mathematical description of local membrane shapes

The local geometry of a 2D surface, Γ, in a 3D space is given by two principal curvatures, C_1 and C_2, which measure the maximal and the minimal curvature of all curvatures appearing in different directions from a point. In differential geometry, local curvatures are usually expressed in terms of the mean curvature, $H = C_1 + C_2$, and Gaussian curvature, $K = C_1C_2$. Here, positive and negative values of H coincide with the widely used expressions outward, or positively, and inward, or negatively, curved, respectively. However, even if the Gaussian curvature, K, is less intuitive than H, its values play an equally important role in most frequent membrane geometries (cf. Fig. 2). In the case of a bud neck, it is the negative Gaussian curvature that describes the geometry. In a perfect saddle geometry, C_1 and C_2 are equal in absolute value with different signs, so that H vanishes.

Static model based on free energies

Our model is based on a generalization of the widely used curvature-dependent Helfrich energy, $\mathcal{F}_{\mathrm{H}}$ (34), which can be derived assuming isotropic dependence of the energy on membrane curvature, the latter given by the principal curvatures C_1 and C_2: expansion in Taylor series of the unknown energy functional $\mathcal{F}_{\mathrm{real}}(C_1, C_2)$ up to the second order yields

$$\mathcal{F}_{\mathrm{real}} \approx \mathcal{F}_{\mathrm{H}} = \int_{\Gamma} \left(\frac{\kappa}{2}(H - H_0)^2 + \kappa_{\mathrm{G}} K \right) ds, \qquad (1)$$

with bending rigidity κ, Gaussian bending rigidity κ_{G}, mean curvature $H = C_1 + C_2$, Gaussian curvature $K = C_1C_2$, spontaneous curvature H_0, and surface measure ds. Here, H_0 is phenomenologically introduced to reflect the preferred mean curvature of the membrane, which can be nonzero, e.g., if membrane components are wedge-shaped. Deviations of the mean curvature, H, from H_0 are elastically penalized.

However, if high local curvatures are considered (such as intrinsic ESCRT curvatures), the use of Helfrich energy terms of higher than quadratic order in the principal curvatures can be necessary. Such terms are required to allow an appropriate energetic description of saddle-shaped membrane constituents. As an example, let us assume a protein locally imposing a perfect saddle shape on the membrane. This means that the membrane energy should be locally minimal for certain principal curvatures, $\tilde{C}_2 = -\tilde{C}_1$ (or equivalently, for certain mean and Gaussian curvature values $H_0 = 0$ and $K_0 < 0$) and should increase if we bend the membrane in at least one of the principal directions from its preferred curvature. However, the conventional Helfrich energy, $\mathcal{F}_{\mathrm{H}}$, does not satisfy these requirements: Assuming, for simplicity, that $\kappa/2 = \kappa_{\mathrm{G}} = 1$, for the above-mentioned minimal configuration, we obtain $\mathcal{F}_{\mathrm{H}} = -\tilde{C}_1^2$. If we now locally deform the membrane, e.g., setting $\tilde{C}_2^{\mathrm{new}} = -(3/2)\tilde{C}_1$, we obtain an even lower energy value, $\mathcal{F}_{\mathrm{H}} = -(5/4)\tilde{C}_1^2$. Hence, $\mathcal{F}_{\mathrm{H}}$ decreases, although we deform the membrane from its preferred shape, which is a result of the fact that Eq. 1 is linear in K.

Thus, in the following, we use the phenomenologically motivated generalization $\mathcal{F}_K$ of the Helfrich energy appropriate for energetic description of saddle-shaped membrane constituents. This energy is given by

$$\mathcal{F}_{\mathrm{K}} = \int_{\Gamma} \left(\frac{\kappa}{2}(H - H_0)^2 + \frac{\widehat{\kappa}_{\mathrm{G}}}{2}(K - K_0)^2 \right) ds. \qquad (2)$$

Here, the second Gaussian rigidity, $\widehat{\kappa}_G$, weights deviations of the Gaussian curvature K from the spontaneous Gaussian curvature K_0. Hence, protein shapes can be expressed in terms of H_0 and K_0, where local deviations from these preferred curvatures are elastically penalized. Such a quadratic term in the Gaussian curvature is one of the terms appearing if we expand the Taylor series in the principal curvatures up to the fourth order (considering only those terms that are invariant under arbitrary transformations of the two-dimensional surface coordinates). In the case of a homogeneous membrane, we identify $-\widehat{\kappa}_{\mathrm{G}}K_0$ with the usual Gaussian curvature modulus, κ_{G}.

Finally, we assume that macroscopic mechanical parameters may depend on the local composition of membrane molecules (the latter described by the order parameter ϕ; cf. next section), as well as possible direct isotropic attractions among membrane molecules (cf. our previous study (33)). This leads to the free energy

$$\mathcal{F} = \int_{\Gamma} \left(\frac{\kappa(\phi)}{2}(H - H_0(\phi))^2 + \frac{\widehat{\kappa}_{\mathrm{G}}(\phi)}{2}(K - K_0(\phi))^2 \right) ds + \mathcal{F}_{\mathrm{CH}}, \qquad (3)$$

which is used throughout our study. Here, the last term accounts for possible ESCRT clustering and describes the Cahn-Hilliard energy (35), given by

$$\mathcal{F}_{\mathrm{CH}} = \int_{\Gamma} \left(\sigma_{\mathrm{d}} \left(\frac{\xi^2}{2}(\nabla^{\Gamma}\phi)^2 + f(\phi) \right) \right) ds, \qquad (4)$$

with diffuse line tension σ_{d}, transitions length ξ, and double well potential $f(\phi)$ (cf. Supporting Material and Mercker et al. (33)). Finally, in the following, we couple the two bending rigidities κ and $\widehat{\kappa}_{\mathrm{G}}$ by using the general bending rigidity $k(\phi)$, which is defined by $k(\phi) = (\kappa(\phi) + \widehat{\kappa}_{\mathrm{G}}(\phi))/2$.

Local coupling of ESCRTs with membrane mechanics

Local ESCRT concentrations within the membrane are expressed by the order parameter ϕ. If $\phi \approx -1$, then the membrane is locally composed of lipids, and if $\phi \approx 1$, then the membrane is dominated by ESCRT proteins. Since lipids and ESCRT proteins may strongly differ in their mechanical properties, such as shape and stiffness, each macroscopic mechanical modulus h, $h \in \{\kappa, \widehat{\kappa}_{\mathrm{G}}, H_0, K_0\}$, is a function of the order parameter ϕ, so $h = h(\phi)$. Each function h is chosen so that $h(1) = h^{\mathrm{P}}$ and $h(-1) = h^{\mathrm{L}}$, where h^{L} and h^{P} are the mechanical moduli of the pure lipids and proteins, respectively. In particular, for each $h \in \{\kappa, \widehat{\kappa}_{\mathrm{G}}, H_0, K_0\}$ we set $h = a - b\tanh(\phi)$ with $b > 0$, which was recently determined from molecular dynamical simulations (36).

Dynamical model

Given a certain state of the membrane system, the system evolves in the direction of the steepest descent of the free membrane energy, given by Eq. 3. Assuming an overdamped motion, which is typically valid for molecular systems, dynamics of the membrane surface, $\vec{X}$, and lateral composition, ϕ, are given by the following gradient flows under the constraint of a local area and mass conservation. Hence, minimization of the free energy is driven by 1) local membrane deformations that depend on the local composition; and 2) lateral sorting, which depends on local membrane curvatures. We obtain the following fourth-order nonlinear PDE system:

$$d_t\phi = L_{\phi}\Delta^{\Gamma}\left[\frac{\delta}{\delta\phi}[\mathcal{F}] \right], \qquad (5)$$

$$d_t\vec{X} = -L_X \frac{\delta}{\delta\vec{X}} \left[\mathcal{F} + \int_{\Gamma} \gamma ds \right], \qquad (6)$$

with the local area constraint $\partial_t[\sqrt{g}] = 0$ (see our previous study (33) for details). Here, Δ^Γ is the Laplace-Beltrami operator and L_X and L_ϕ are kinetic coefficients. Furthermore, $\delta/\delta\vec{X}[F]$ and $\delta/\delta\vec{X}[\phi]$ denote the variation of F with respect to $\vec{X}$ and ϕ, respectively, γ is the local Lagrange multiplier modeling local membrane incompressibility, and $\sqrt{g}$ is the surface measure. Further details concerning the derivation of these equations and the detailed calculation of corresponding variations are provided in the Supporting Material, as well as in our previous work (33).

Simulation method

For simulations of Eqs. 5 and 6 we use the finite-element library Gascoigne (38). For time discretization, we apply an adaptive semi-implicit Euler scheme and for spatial discretization a mixed finite-element approach. The membrane surface is discretized using a quadrangular grid with $\geq$16,641 grid points. For all unknown functions, we impose periodic boundary conditions. Computations are performed on a single core (Xeon E5-2690 (Intel, Santa Clara, CA), 2.90 GHz) and it requires ~12 h for one simulation representing 40 ms. Further details regarding the computing scheme are provided in our previous work (33).

Parameter estimation

Protein shape and intrinsic curvature

To translate structural protein data into our continuous description, we calculate intrinsic curvatures of the ESCRT-I/II complex using the geometries of its most frequent conformations (9). We thereby assume that ESCRT-I/II (+ Vps20) structurally fits the bud neck, i.e., we approximate its shape by two elastic tubes that together constitute a saddle shape (Fig. S1 in the Supporting Material and Fig. 1). This description matches structural data showing that rigid-body parts of ESCRT-I/II mainly consist of elongated and partially curved elements (1,6,9,23). Specifically, different parts of the Y-shaped ESCRT-I/II complex show intrinsic curvatures fitting well the curvature directions and magnitudes of the neck region of induced buds (the spoke model (9)). Interestingly, the induction of necklike curvatures has been recently linked to protein regions with significant conformational flexibility (19), also observed for ESCRT-I/II (9).

Consistent with the structural data of Hurley and colleagues (4,9), we assume that one curved tube is given by ESCRT-I plus one copy of the ESCRT-II subunit Vps36 and the other tube is composed of the two ESCRT-II Vps25 subunits (+ Vps20) (see Supporting Material). Since Vps20 is myristoylated at its N-terminus (15,16), it is assumed to strongly interact with membranes (23). Hence, this probably has an impact on curvatures of the ESCRT-I/II complex. However, due to the lack of more detailed corresponding data, we assume that Vps20 does not change local protein curvatures (i.e., it extends existing tubes with the same curvature). As discussed below in detail, we compensate for this and other uncertainties by investigating a more broadly defined parameter space related to ESCRT-I/II shapes rather than a single geometry (see, for example, Fig. 6, *a*, *b*, and *d*).

Intrinsic protein curvatures have been graphically determined by constructing circles with corresponding protein elements. Details of the fitting procedure are provided in the Supporting Material. We finally obtain ESCRT-I/II shapes expressed in terms of the spontaneous Gaussian $K_0^{\mathrm{P}} = -4.33 \times 10^{-4}\,\mathrm{nm}^{-2}$ and spontaneous mean curvature $H_0^{\mathrm{P}} = 2.0 \times 10^{-2}\,\mathrm{nm}^{-1}$, respectively, which have been used for our simulations (if not otherwise stated). The estimated mean curvature value well fits the observation that ESCRT-II + Vps20 favors vesicles of diameter $r =$ 95 nm (22), which corresponds to a mean curvature value of $H = 2.1 \times 10^{-2}\,\mathrm{nm}^{-1}$. Furthermore, the estimated Gaussian curvature is of realistic order, since even stronger K-values have been estimated for ESCRT-related membrane proteins (24).

Nevertheless, we want to point out that K_0^{P} and H_0^{P} are subject to uncertainties for different reasons. 1) The ESCRT-I/II supercomplex appears in 18 different configurations, reaching from compact states to extended conformations (9). Thus, the resulting curvature values are not unambiguous. 2) As mentioned above, amphipathic helix insertion of ESCRT-I/II subunits Vps37 and Vps22 could increase the imposed effective Gaussian curvature to an unknown extent. 3) Conversely, the effective imposed curvatures could be smaller than intrinsic protein curvatures; both converge only if proteins show sufficient intrinsic rigidity and membrane affinity to counteract the preferred curvature of the bilayer (39). 4) Reducing a complicated 3D protein structure to two curvature values and restricting the interactions with the surrounding bilayer to the crossing point of two tubes is a simplification (see also related models (40–42)). Addressing the latter point and following the argumentation of Kralj-Iglic et al. (40), we assume that regions with significant protein-induced membrane distortions are small with respect to the lateral membrane dimensions, so this simplification may be justified.

Thus, we do not restrict our simulations to the above-mentioned specific values of K_0^{P} and H_0^{P}. Instead, we perform additional simulations over a wide range of curvature, stiffness, and line tension values to determine the robustness of the model with respect to final budding patterns, budding directions, and bud sizes (see Figs. 4, 5, and 6).

Finally, we mention that spontaneous mean and Gaussian curvatures in this study are not imposed on the membrane as a global intrinsic curvature. Instead, we couple local protein (ESCRT) concentrations with local membrane curvature, assuming certain K_0^{P} and H_0^{P} values for protein-rich regions, but always setting $K_0^{\mathrm{L}} = H_0^{\mathrm{L}} = 0$ for membrane lipids (for further details, see the section Local coupling of ESCRTs with membrane mechanics, above). Furthermore, the approach presented here assumes that anisotropic proteins always orient in-plane such that it is energetically favorable.

Membrane rigidities

In all simulations, for the macroscopic bending rigidity, κ^{L}, of a membrane locally composed of lipids, we set $\kappa^{\mathrm{L}} = 12\,k_{\mathrm{B}}\,T$, which is a typical value for lipid bilayers. Since we do not know whether ESCRT protein complexes locally influence membrane stiffness (which could in principle induce either an increase or a decrease in rigidity (43–46)), we set the macroscopic protein bending rigidity at $\kappa^{\mathrm{P}} = \kappa^{\mathrm{L}}$ unless otherwise stated. This assumption means that local ESCRT accumulations do not change the membrane stiffness. Nonetheless, we also evaluate an effect of ESCRTs on membrane stiffness (cf. Results and Discussion).

Experimentally determined values for the second Gaussian rigidity, $\widehat{\kappa}_{\mathrm{G}}^{\mathrm{P}}$ and $\widehat{\kappa}_{\mathrm{G}}^{\mathrm{L}}$, are not yet available. However, measurements of the usual Gaussian curvature modulus, κ_{G}, show that it is of the same order as κ (47,48). Since (in the case of a homogeneous membrane) we can identify $-\widehat{\kappa}_{\mathrm{G}}\,K_0$ with κ_{G}, we choose $\widehat{\kappa}_{\mathrm{G}}^{i} \approx -\kappa^{i}/K_0^{\mathrm{P}}$ by setting $\widehat{\kappa}_{\mathrm{G}}^{i} \equiv \kappa^{i}\,\mu\mathrm{m}^2$, $i \in \{l, p\}$. Thus, we always ensure that $\widehat{\kappa}_{\mathrm{G}}^{i}$ is of realistic order if we consider locally imposed Gaussian curvatures $K_0^{\mathrm{P}} = -4.33 \times 10^{-4}\,\mathrm{nm}^{-2}$. This direct comparison between κ_{G} and $\widehat{\kappa}_{\mathrm{G}}$ implies for our special case that κ_{G} is positive, since $\kappa_{\mathrm{G}} = -\widehat{\kappa}_{\mathrm{G}}^{i}K_0^{\mathrm{P}} > 0$. This is in principle possible (48) but is not usually the case (47). Interestingly, more general numerical investigations of the energy presented here reveal that $\widehat{\kappa}_{\mathrm{G}}$ is qualitatively comparable to $-\kappa_{\mathrm{G}}$ rather than to κ_{G} (see Supporting Material). This also becomes obvious if we take a closer look at the classical Helfrich energy compared to the higher-order energy presented here: In Eq. 1, the linear term $\kappa_{\mathrm{G}}\int K ds$ requires a negative κ_{G} to energetically penalize negative Gaussian curvatures (e.g., saddle-like deformations in which H vanishes). In contrast, we need $\widehat{\kappa}_{\mathrm{G}} > 0$ to achieve the same effect (relative to K_0) with $(\widehat{\kappa}_{\mathrm{G}}/2)\int (K - K_0)^2 ds$ from Eq. 2. To additionally ensure that this higher-order energy reproduces typical effects associated with the classical linear Gaussian curvature term, we perform additional analytical and numerical studies. For example, considering biphasic vesicles, we find that gradients in $\widehat{\kappa}_{\mathrm{G}}$ induce typical shifts of necklike structures in the direction of the phase with the lower rigidity, as described for gradients in (negative) values of κ_{G} (32,49) (for more details, see the Supporting Material as well as Fig. S2).

Dynamical parameters

Regarding the Cahn-Hilliard part of the energy accounting for possible ESCRT-clustering (Eq. 4), we always assume $\xi = 10$ nm and $f(\phi) = 9/32(\phi^2 - 1)^2$ for $\phi \in [-1,1]$, such that the diffuse line-tension value σ_d is uniquely determined by the sharp line-tension value σ due to $\sigma = \xi\sigma_d$ (see the Supporting Material). To include the effect of short-range repulsion between membrane molecules, we also apply the increased double-well potential $\widehat{f}(\phi) = 50 \times f(\phi)$ for ϕ outside $[-1,1]$.

For the line tension, σ, between ESCRTs and lipids, we assume a relatively weak value of $\sigma = 0.005$ pN unless otherwise stated. This is motivated by the fact that ESCRT-I and ESCRT-II alone build no clusters (3) or only very small clusters (21) (microdomains) in membranes, and line-tension effects are in general assumed to be not large enough to drive budding and scission in the case of ESCRT-induced budding (21). Hence, we use values that are orders of magnitude lower than values determined during vesicle budding (e.g., $\sigma \approx 1$ pN in Baumgart et al. (50)).

Dynamics of ESCRT-I/II within the membrane are given by Eq. 5, in which the mobility, L_ϕ, is assumed to be constant, scaling inversely with the viscosity of the membrane (33,36). The corresponding diffusion coefficient D is given by $D = L_\phi\,\sigma_d$, which may depend on the (lateral) size of proteins within the membrane plane (51), expressed by a lateral radius, R. Based on recent structural data (9), a rough approximation of an averaged ESCRT-I/II radius yields $R_{ESCRT} \approx 15$ nm, leading to a corresponding diffusion coefficient (51) of $D_{ESCRT} \approx 3\ \mu m^2\ s^{-1}$. Hence, in the simulations presented here, we assume the mobility $L_\phi = 3\ \mu m^2(\sigma_d\ s)^{-1}$, leading to a molecular diffusion coefficient of $D = 3\ \mu m^2\ s^{-1}$.

Furthermore, the dynamics of surface deformations are given by Eq. 6. However, estimates for L_X do not exist in the literature so far. Since MD simulations frequently show that lateral dynamics are of faster order than surface deformations, in all simulations, we set $L_X = 0.1 \times L_\phi$. In addition, we verify numerically that different magnitudes of L_X lead to similar final patterns (results not shown).

RESULTS AND DISCUSSION

Results of numerical simulations

In the following, we consider a model membrane patch of 1 μm^2 containing lipids and membrane-associated ESCRT-I/II proteins. Constant initial distribution of the proteins follows experiments (3). We set $\phi \equiv -0.2$, which corresponds to the ESCRTs covering 40% of the membrane surface. Furthermore, the simulations are started from an arbitrarily curved membrane; the z axis of the membrane surface is generated anew in each simulation and stochastically deflected with a uniform distribution in the interval $[-2$ nm,2 nm] (Fig. 3 *b*).

Our simulations show that the shape of ESCRT complexes is sufficient to yield structures resembling those found in experiments (Fig. 3 *a*). We observe a spontaneous creation of membrane buds with the highest ESCRT concentration radially organized in the bud-neck region (bud-neck scaffolding), a medium protein concentration in the surroundings of buds, and no ESCRT proteins at the bud surface (Fig. 3, *b–e*). These results fit well the theoretical predictions of Iglic et al. (42), in which a lateral reorganization of anisotropic membrane constituents leads to spontaneous bud-neck formation in membrane tubes. Using the example of ESCRTs, our results reveal that this mechanism can even produce vesicles from an almost flat membrane without relying on other shaping components.

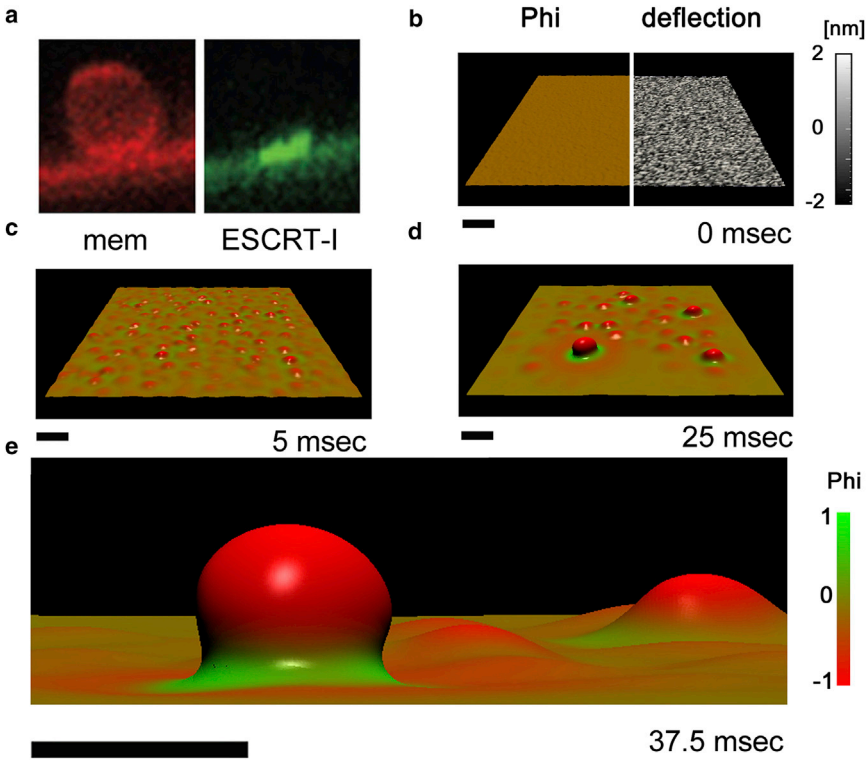

FIGURE 3 Membrane budding driven by the ESCRT shape-induced bud-neck scaffolding. (*a*) Image from the experimental study of Hurley and colleagues (1). (*b–e*) Based on a stochastically deflected membrane, deformation-mediated sorting of saddle-shaped ESCRTs leads to membrane structures very similar to those observed in experiments (*a*). Green and red colors correspond to high and low ESCRT concentrations, respectively. Scale bars, 100 nm. To see this figure in color, go online.

Bud sizes in vivo, in vitro, and in silicio

Diameters of simulated buds show an average size of $\approx$100 nm (Fig. 3 *e*), which is in the range of 40–100 nm determined in vivo (52). We notice that the simulated bud diameters are slightly overestimated, since the simulations stop before complete budding takes place. In contrast, ESCRT-I/II-induced buds in giant unilamellar vesicles (GUVs) appear to be significantly larger, with a diameter of $d \approx 2\ \mu$m (3). However, GUVs and early endosomes distinctly differ in their membrane stiffnesses (20): Bending rigidities in early endosomes are about $5k_BT$ (53), which is distinctly smaller than bending rigidities usually measured in GUVs (54). Hence, we investigate numerically the impact of lipid bilayer stiffness, k^L, on bud sizes while keeping ESCRT rigidity, k^P, constant. Since full budding is prevented due to lateral tensions (cf. Dependency of bud neck scaffolding on protein shapes and line tension), especially for larger buds, we define the reduced bud size, d_r, by the maximal lateral diameter of a (cup-shaped) bud, evaginating 75 nm from the midplane. Indeed, we find that the average bud diameter growths linearly with increasing lipid bilayer stiffness with a rate of ~7 nm/k_BT (see Fig. 6 *c*).

Based on the same bending rigidity difference between endosomes and GUVs, Różycki et al. (20) recently provided an alternative explanation, attributing bud-size differences in vivo and in vitro to the impact of lipid phase segregation, possibly involved in ESCRT-induced budding. Assuming that the line tension at lipid domain boundaries is the main force that drives budding, those authors also observed that the bud radius scales linearly with lipid bending rigidity. This mechanism (which is not considered within the model presented here) could play an additional role in determining final ESCRT-induced bud sizes.

ESCRT shapes and budding directions

Microscopical studies of in vivo and in vitro systems reveal that ESCRT-induced budding is strongly directed: Budding always appears in the inward direction of corresponding membrane components (3,52). Our simulations reveal that this directional budding also can be a result of ESCRT shape: Considering the protein orientation as proposed in Boura et al. (9), we observe the same budding direction in nearly all simulations, which fits the inward budding direction consistently observed in experiments. Symmetry arguments suggest that this inward direction is also determined by the sign of the spontaneous curvature, H_0^P. This parameter reflects differences in the two principal curvatures of the protein saddle shape (Fig. 4) and provides the only up-down asymmetry in the simulated system. Although this influence on budding direction under reflection of system asymmetry is self-evident from a theoretical point of view, the question of how budding direction depends on the sign of H_0^P is less intuitively accessible. Hence, we

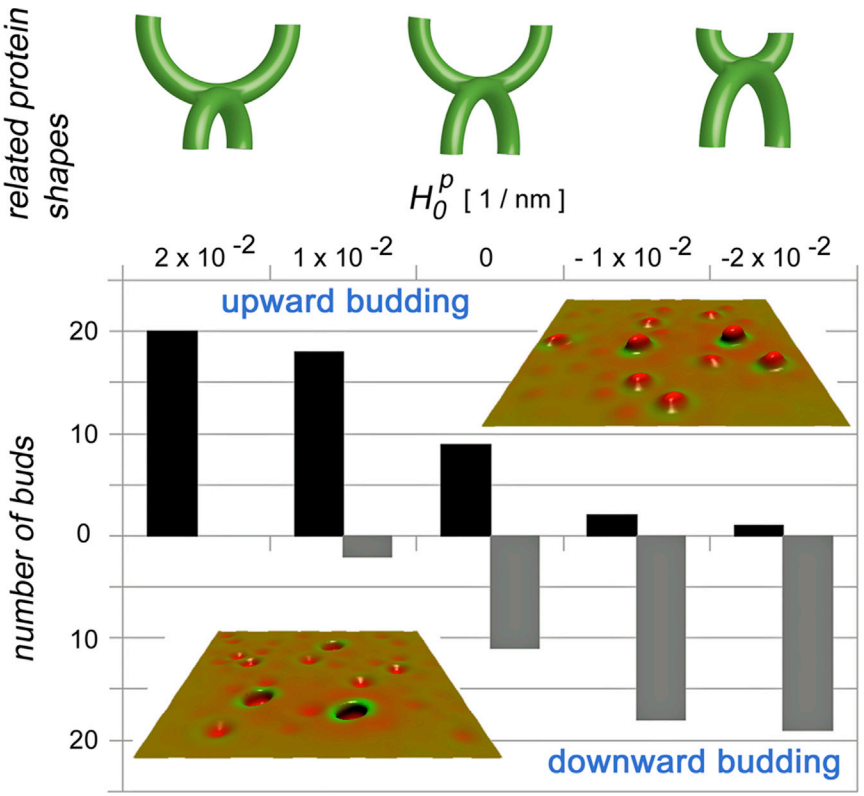

FIGURE 4 ESCRT shape determines budding direction. Budding direction for different values of the spontaneous protein curvature H_0^P has been analyzed (20 buds for each H_0^P value, keeping K_0^P constant). Related protein shapes are shown in green. To see this figure in color, go online.

perform 20 simulations for different values of H_0^P and measure the direction of the furthest developed bud. Our results show that the sign of the bud surface's (mean) curvature tends to be opposed to the sign of H_0^P (Fig. 4).

Dependency of bud-neck scaffolding on protein shapes and line tension

In all simulations, bud-neck scaffolding appears to depend critically on 1) the protein shape, and 2) a weak line tension. In particular, we find that values of $\sigma \geq 0.01$ pN prevent the establishment of ESCRT rings and membrane buds, leading instead to closed protein clusters (see Figs. 6 *b* and 7, *a–c*). To investigate how sensitively bud-neck scaffolding depends on protein shape, we performed various simulations using different values of K_0^P and H_0^P, respectively. A small selection (including exemplified corresponding protein shapes) is shown in Fig. 5. Our results reveal that the formation of a bud with a protein ring in its neck region is strongly coupled to a negative value of K_0 (Fig. 5, *d* and *e*). That is, the two elastic tubes representing the protein have opposite curvatures, constituting together a saddle-shaped complex.

However, in the case of nonnegative K_0 values, different patterns appear that are in good accordance with previous data: In the case of vanishing spontaneous protein curvatures H_0^P and K_0^P, no distinct patterning appears within the considered simulation time (Fig. 5 *a*). This is related to the fact that patterning processes are significantly slower if mechanical moduli do not differ between the different membrane components (36).

In contrast, an imposed positive protein mean curvature, $H_0^P > 0$ (with vanishing K_0^P) leads to clearly visible, partially elongated protein patches (Fig. 5 *b*). Actually, a spontaneous formation of scaffolded 3D membrane tubules (tubulation) would be expected for these parameters (cf. Fig. 2 *a* and Lipowsky (58)). This is probably prevented due to lateral tensions: in our simulation, nearly all proteins, i.e., 40% of the membrane surface, form clusters. Hence, a further evagination of all these clusters would require more membrane area than provided by the initial conditions, and additional area cannot be pulled from domain boundaries. Thus, full tubulation is prevented due to lateral tensions stabilizing incomplete buds/tubules (59).

Finally, for positive K_0^P and H_0^P values, we observe the formation of various small cup-shaped buds, where proteins cover the entire bud surface (Fig. 5 *c*). However, this observation matches with various theoretical and experimental results, e.g., considering clathrin-induced budding (10,60,61). Also here, full budding in our simulations is probably prevented because there is an insufficient amount of membrane area inducing lateral tension.

To examine more generally the conditions under which the system stabilizes bud necks, as opposed to forming uniform aggregates, we also explore and plot membrane behavior in terms of two different phase diagrams (Fig. 6, *b* and *d*). First, the spontaneous protein mean H_0^P and Gaussian curvature K_0^P are used as control parameters (keeping $\sigma = 0.005$ pN). We find that bud-neck scaffolding does not sensitively depend on H_0^P, but only on K_0^P. Especially for all values $K_0^P < -3.5 \times 10^{-4}\,\mathrm{nm}^{-2}$, proteins are found to be organized in bud-neck regions (Fig. 6 *d*).

Second, the line tension, σ, and the spontaneous protein Gaussian curvature, K_0^P, are used as control parameters (keeping $H_0^P = 0$). We find that σ and K_0^P behave antagonistically in this process: strong intrinsic protein curvatures support the formation of stabilized bud necks, whereas strong line tensions lead to the formation of uniform protein aggregates. This phase transition is best described by a linear fit (at least within the considered parameter range): bud-neck scaffolding appears only if $K_0^P < (-2.1 \times 10^{-4} - 1.65 \times 10^{-2}\,\sigma\,\mathrm{pN}^{-1})\,\mathrm{nm}^{-2}$ holds (Fig. 6 *b*).

From a molecular point of view, these observations reflect the antagonistic behavior of direct protein attractions versus

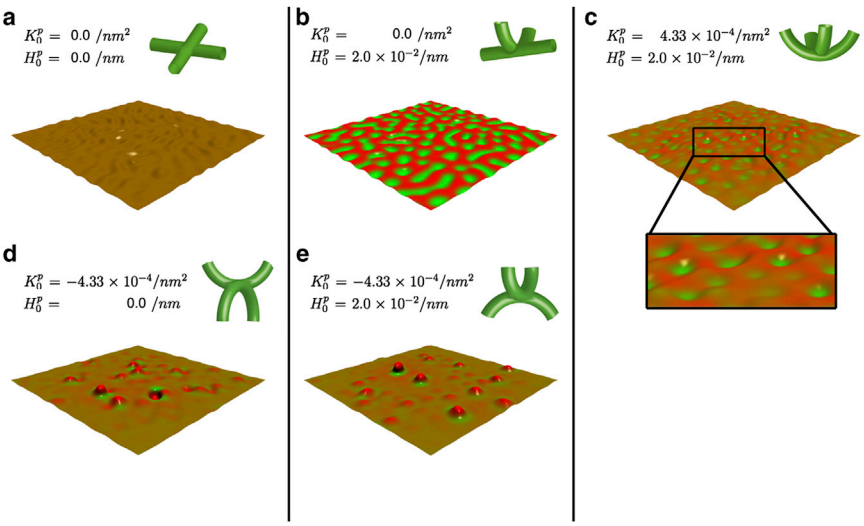

FIGURE 5 Patterns resulting from different protein shapes fitting to planar (*a*), tubular (*b*), spherical (*c*), and bud neck-shaped (*d* and *e*) membranes. All snapshots represent patterns after 30 ms. Protein shapes are expressed in terms of H_0^P and K_0^P; related sample protein shapes are shown in green. Inset in (*c*) is an enlargement of the boxed area in the snapshot. To see this figure in color, go online.

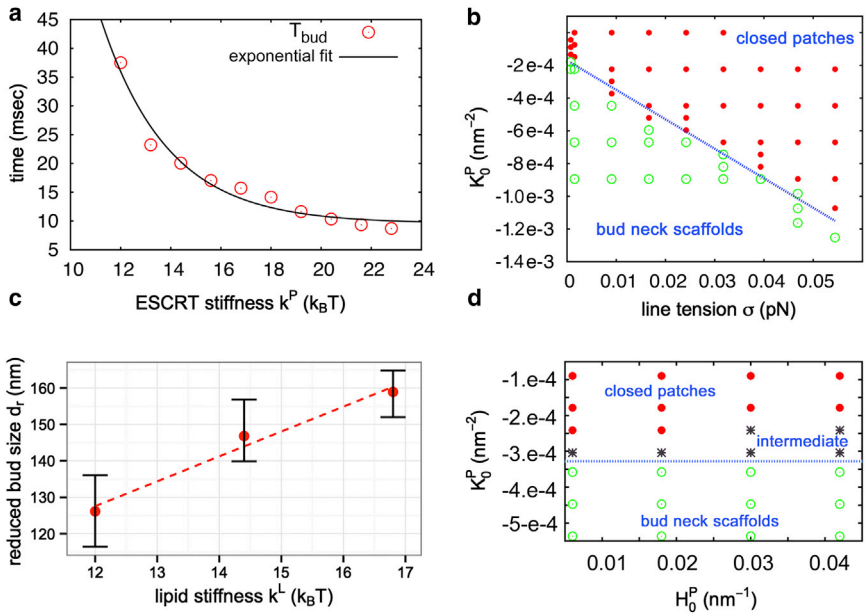

FIGURE 6 (*a*) Velocity of membrane budding depends on the influence of ESCRTs on bending rigidity, k^{P}: The time to budding, T_{bud}, decays exponentially with increasing k^{P} (*red dots*, values from simulations; *black line,* exponential fit of the kind $a + b\exp(-ck)$). (*b*) Phase diagram with control parameters K_0^{P} and σ (with $H_0^{\mathrm{P}} = 0$). Bud-neck scaffolding appears for protein Gaussian curvature values with $K_0^{\mathrm{P}} < (-2.1 \times 10^{-4} - 1.65 \times 10^{-2}\ \sigma\ \mathrm{pN}^{-1})\ \mathrm{nm}^{-2}$. (*c*) Bud size increases linearly with lipid bending rigidity κ^{L} (error bars indicate 95% confidence intervals). (*d*) Phase diagram with control parameters K_0^{P} and H_0^{P} (with $\sigma = 0.005$ pN). Bud-neck scaffolding does not sensitively depend on H_0^{P}. (In both phase diagrams (*b* and *d*), red dots correspond to simulations showing closed protein patches, green circles to bud-neck scaffolds, and black asterisks to intermediate patterns.) To see this figure in color, go online.

membrane-mediated sorting: Where direct (isotropic) molecule attractions favor the establishment of closed clusters with small domain boundaries (35), membrane-mediated sorting minimizes energetic/entropic penalties arising from the local interplay between proteins and the surrounding membrane. In the latter case, energetically preferred protein patterns depend on the exact underlying physics that dominate protein-membrane interactions: if local structural membrane perturbations (such as hydrophobic mismatch or imposed curvatures) are isotropic, resulting protein clusters are usually closed (25,27,62). In contrast, in the study presented here, imposed negative Gaussian curvatures are anisotropic, thus leading to protein rings instead of uniform aggregates. These results fit well with previous studies indicating that the formation of bud necks can be driven by a coupling between local membrane curvature and the lateral organization of anisotropic membrane constituents (40–42).

Within these bud necks, ESCRT molecules are assumed to show a higher orientational order than in line-tension-dominated clusters: imposed negative Gaussian curvatures lead (due their inherent anisotropy, i.e., $C_1 \neq C_2$) to an oriented alignment of similarly shaped proteins (see Fig. 7, *d* and *e*) and finally to a catenoid structure. In contrast, we observe that the membrane in line-tension-dominated clusters prefers a flat geometry (i.e., $C_1 = C_2 = 0$; see also Fig. 7 *c*), which makes protein orientations arbitrary from an energetic point of view.

In terms of minimizing a free energy, the above-mentioned antagonistic behavior between line tension and

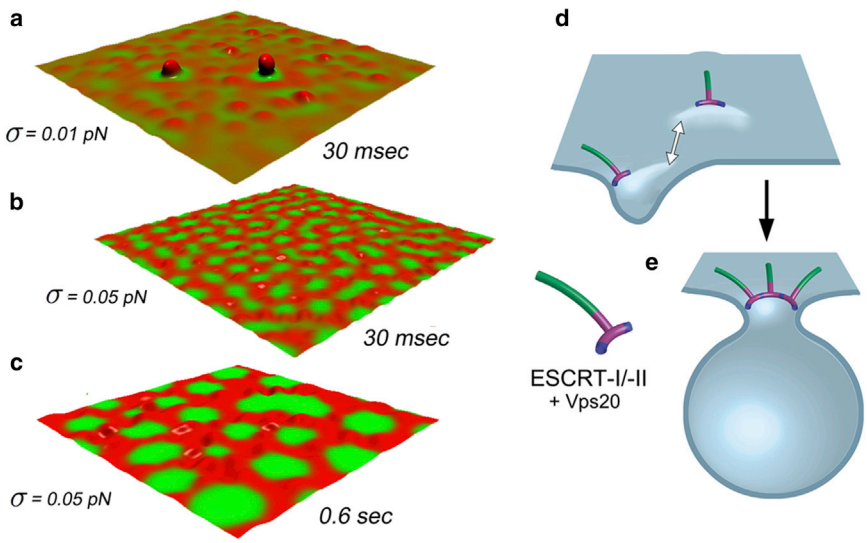

FIGURE 7 Effect of the line tension and a schematic model of ESCRT-induced budding. (*a–c*) Above a critical value, the line tension, σ, prevents ESCRT-induced bud-neck scaffolding, instead leading to protein clusters. (*d* and *e*) Hence, deformation-mediated attractions are assumed to be the driving force in budding: ESCRTs locally impose their shape, which attracts similarly shaped proteins (*white arrow*) (*d*), leading to a protein ring that forces the membrane to bud (*e*). To see this figure in color, go online.

intrinsic protein curvature reflects the simultaneous minimization of the Helfrich-type and the Cahn-Hilliard energy (cf. Eq. 3), where both energy terms favor different minimum configurations.

Possible role of structural flexibility in bud formation

As mentioned above, recent results demonstrate that the ESCRT-I/II complex shows high structural flexibility rather than a single distinct rigid geometry (9). Although the model presented here in principle allows for local deformation of ESCRT protein shapes from their preferred geometry, it does not account for different preferred conformations at the same time or during one simulation. Instead, we account for structural flexibility by investigating parameters related to protein shapes and stiffness in different simulations (cf. Fig. 6).

Regarding the possible function of the structural ESCRT-I/II flexibility, two extreme cases are imaginable during bud formation: 1) different stable configurations existing side by side in a more or less fixed ratio, each shape constituting one building block of the final shape; and 2) each ESCRT-I/II complex changing flexibly between different configurations, adapting to each particular process in membrane remodeling or cargo sorting. However, the first possibility seems less likely, since it is assumed that ESCRT-I/II complexes are finally arranged in a symmetric manner (i.e., the spoke model), which would not require such a structural heterogeneity. In contrast, the second scenario has been examined recently by assigning different conformations to certain steps in cargo sorting (9). In the context of membrane remodeling, it is conceivable that these conformational changes are induced by the dynamic interplay between ESCRT-I/II and the membrane. This means that small energy barriers linked to these changes may be crossed by mutual ESCRT interactions and/or in interplay with the surrounding membrane geometry. In return, certain steps in membrane remodeling also might energetically favor or require particular ESCRT-I/II conformations.

The effect of membrane stiffening and weakening due to ESCRTs

Besides imposing their shapes on the membrane, membrane proteins may also increase or decrease the local membrane bending rigidity (43–46). To investigate how this affects ESCRT-induced budding, we performed simulations with different protein bending rigidities, k^{P}, increasing stepwise from 12 $k_{\mathrm{B}}T$ to 23 $k_{\mathrm{B}}T$ (keeping $k^{\mathrm{L}} = 12k_{\mathrm{B}}T$). To ensure better comparability, here, we use the same initial conditions for all corresponding simulations. We find that resulting patterns do not significantly differ from each other (data not shown). In contrast, dynamics of the system appear to be strongly influenced by gradients in k^{P}: The time to bud development, T_{bud}, exponentially decreases with increasing ESCRT stiffness (Fig. 6 *a*). Similar results have been recently reported for classical membrane budding and sorting mechanisms (33,36).

CONCLUSIONS

Our simulations suggest that ESCRT-I/II-induced bud-neck scaffolding can be driven by the dynamic interplay between protein shapes and membrane curvature: ESCRT locally deforms the surrounding membrane, which attracts other similarly shaped proteins, leading to a protein ring, which enforces budding (cf. Fig. 7, *d* and *e*). Our model qualitatively and quantitatively reproduces most of the experimental observations of ESCRT-induced budding, such as membrane shape, lateral protein patterns, budding direction, and bud size in vivo and in vitro.

For a further justification of the model presented here, it will be desirable to estimate corresponding line tensions induced by ESCRT-I/II clustering, e.g., evaluated from domain nucleation rates on supported bilayers (63). Furthermore, it will be of great interest to discover to what extent different parts of the ESCRT-I/II complex (such as structural elements or cationic helices) contribute to its affinity to negative Gaussian curvatures. This might be accomplished using different deletion mutations of ESCRT-I/II to subsequently investigate corresponding budding behavior in GUVs (3) or lateral ESCRT organization on corrugated curved membranes (64) showing regions of negative Gaussian curvature. An alternative way for a further validation of the proposed model will be the use of coarse-grained MD techniques, e.g., to estimate elastic parameters (19,65) using simplified shapes of the ESCRT-I/II complex. Furthermore, the relation between lipid bilayer bending rigidity and bud size (as proposed in this study, as well as in that of Różycki et al. (20)) can be examined by modifying the interplay between GUV bending rigidity (54) and ESCRT-induced bud formation.

An interesting future extension of the model presented here may involve including the lipid phase separation induced by ESCRT proteins, as proposed by Różycki et al. (20): In this context, it will be desirable to confirm ESCRT-I/II-induced lipid phase separation (e.g., using the methods of Baumgart et al. (50) in combination with ESCRT-I/II) and to estimate corresponding line tensions.

In contrast to previously described membrane-mediated patterning processes, (25,27,62), in the model presented here, strong line tensions prohibit the deformation of mediated patterns. Hence, our results reveal that membrane-mediated sorting not only may serve as an alternative for direct protein attractions (25), but must be seen as a self-contained and even irreplaceable mechanism in the process of protein sorting and bud formation.

SUPPORTING MATERIAL

Supporting Materials and Methods and two figures are available at http://www.biophysj.org/biophysj/supplemental/S0006-3495(14)04819-X.

SUPPORTING CITIATIONS

References (66–78) appear in the Supporting Material.

ACKNOWLEDGMENTS

The authors greatly thank Dr. Mark Peletier and Dr. Dirk Hartmann for fruitful discussions and Lisa Kolb and Dr. Susanne Krömker for visualization.

Both authors were supported by the European Research Council Starting Grant Biostruct (No. 210680) and the Emmy Noether Program of the Deutsche Forschungsgemeinschaft.

REFERENCES

1. Hurley, J. H., E. Boura, …, B. Różycki. 2010. Membrane budding. *Cell.* 143:875–887.
2. Kirchhausen, T. 2000. Three ways to make a vesicle. *Nat. Rev. Mol. Cell Biol.* 1:187–198.
3. Wollert, T., and J. H. Hurley. 2010. Molecular mechanism of multivesicular body biogenesis by ESCRT complexes. *Nature.* 464:864–869.
4. Hurley, J. H., and P. I. Hanson. 2010. Membrane budding and scission by the ESCRT machinery: it's all in the neck. *Nat. Rev. Mol. Cell Biol.* 11:556–566.
5. Hurley, J. H. 2010. The ESCRT complexes. *Crit. Rev. Biochem. Mol. Biol.* 45:463–487.
6. Williams, R. L., and S. Urbé. 2007. The emerging shape of the ESCRT machinery. *Nat. Rev. Mol. Cell Biol.* 8:355–368.
7. Rusten, T. E., T. Vaccari, and H. Stenmark. 2012. Shaping development with ESCRTs. *Nat. Cell Biol.* 14:38–45.
8. Wollert, T., C. Wunder, …, J. H. Hurley. 2009. Membrane scission by the ESCRT-III complex. *Nature.* 458:172–177.
9. Boura, E., B. Różycki, …, J. H. Hurley. 2012. Solution structure of the ESCRT-I and -II supercomplex: implications for membrane budding and scission. *Structure.* 20:874–886.
10. Graham, T. R., and M. M. Kozlov. 2010. Interplay of proteins and lipids in generating membrane curvature. *Curr. Opin. Cell Biol.* 22:430–436.
11. Mayers, J. R., and A. Audhya. 2012. Vesicle formation within endosomes: an ESCRT marks the spot. *Commun. Integr. Biol.* 5:50–56.
12. Otegui, M. S., R. Buono, …, H. Roschzttardtz. 2012. ESCRT-Dependent Sorting in Late Endosomes. *In* Endocytosis in plants, 1st ed.. J. Šamaj, editor. Springer, New York, pp. 249–270.
13. Kostelansky, M. S., C. Schluter, …, J. H. Hurley. 2007. Molecular architecture and functional model of the complete yeast ESCRT-I heterotetramer. *Cell.* 129:485–498.
14. Im, Y. J., and J. H. Hurley. 2008. Integrated structural model and membrane targeting mechanism of the human ESCRT-II complex. *Dev. Cell.* 14:902–913.
15. Babst, M., D. J. Katzmann, …, S. D. Emr. 2002. Escrt-III: an endosome-associated heterooligomeric protein complex required for mvb sorting. *Dev. Cell.* 3:271–282.
16. Yorikawa, C., H. Shibata, …, M. Maki. 2005. Human CHMP6, a myristoylated ESCRT-III protein, interacts directly with an ESCRT-II component EAP20 and regulates endosomal cargo sorting. *Biochem. J.* 387:17–26.
17. Rossman, J. S., X. Jing, …, R. A. Lamb. 2010. Influenza virus M2 protein mediates ESCRT-independent membrane scission. *Cell.* 142:902–913.
18. Schmidt, N. W., A. Mishra, …, G. C. L. Wong. 2011. Criterion for amino acid composition of defensins and antimicrobial peptides based on geometry of membrane destabilization. *J. Am. Chem. Soc.* 133:6720–6727.
19. Braun, A. R., E. Sevcsik, …, J. N. Sachs. 2012. α-Synuclein induces both positive mean curvature and negative Gaussian curvature in membranes. *J. Am. Chem. Soc.* 134:2613–2620.
20. Różycki, B., E. Boura, …, G. Hummer. 2012. Membrane-elasticity model of Coatless vesicle budding induced by ESCRT complexes. *PLOS Comput. Biol.* 8:e1002736.
21. Boura, E., V. Ivanov, …, J. H. Hurley. 2012. Endosomal sorting complex required for transport (ESCRT) complexes induce phase-separated microdomains in supported lipid bilayers. *J. Biol. Chem.* 287:28144–28151.
22. Fyfe, I., A. L. Schuh, …, A. Audhya. 2011. Association of the endosomal sorting complex ESCRT-II with the Vps20 subunit of ESCRT-III generates a curvature-sensitive complex capable of nucleating ESCRT-III filaments. *J. Biol. Chem.* 286:34262–34270.
23. Im, Y. J., T. Wollert, …, J. H. Hurley. 2009. Structure and function of the ESCRT-II-III interface in multivesicular body biogenesis. *Dev. Cell.* 17:234–243.
24. Schmidt, N. W., A. Mishra, …, G. C. L. Wong. 2013. Influenza virus A M2 protein generates negative Gaussian membrane curvature necessary for budding and scission. *J. Am. Chem. Soc.* 135:13710–13719.
25. Reynwar, B. J., G. Illya, …, M. Deserno. 2007. Aggregation and vesiculation of membrane proteins by curvature-mediated interactions. *Nature.* 447:461–464.
26. Gumbart, J., Y. Wang, …, K. Schulten. 2005. Molecular dynamics simulations of proteins in lipid bilayers. *Curr. Opin. Struct. Biol.* 15:423–431.
27. Hanulová, M., and M. Weiss. 2012. Membrane-mediated interactions—a physico-chemical basis for protein sorting. *Mol. Membr. Biol.* 29:177–185.
28. Šarić, A., and A. Cacciuto. 2012. Mechanism of membrane tube formation induced by adhesive nanocomponents. *Phys. Rev. Lett.* 109:188101.
29. Grime, J. M. A., and G. A. Voth. 2014. Highly scalable and memory efficient ultra-coarse-grained molecular dynamics simulations. *J. Chem. Theory Comput.* 10:423–431.
30. Ingolfsson, H., C. Lopez, …, S. Marrink. 2014. The power of coarse-graining in biomolecular simulations. *Wiley Interdiscip. Rev. Comput. Mol. Sci.* 4:225–248.
31. Brown, F. L. H. 2008. Elastic modeling of biomembranes and lipid bilayers. *Annu. Rev. Phys. Chem.* 59:685–712.
32. Baumgart, T., S. Das, …, J. T. Jenkins. 2005. Membrane elasticity in giant vesicles with fluid phase coexistence. *Biophys. J.* 89:1067–1080.
33. Mercker, M., A. Marciniak-Czochra, …, D. Hartmann. 2013. Modeling and computing of deformation dynamics of inhomogeneous biological surfaces. *SIAM J. Appl. Math.* 73:1768–1792.
34. Helfrich, W. 1973. Elastic properties of lipid bilayers: theory and possible experiments. *Z. Naturforsch. C.* 28:693–703.
35. Cahn, J., and J. Hilliard. 1958. Free energy of a nonuniform system. I. Interfacial free energy. *J. Chem. Phys.* 28:258–267.
36. Mercker, M., M. Ptashnyk, …, W. Jäger. 2012. A multiscale approach to curvature modulated sorting in biological membranes. *J. Theor. Biol.* 301:67–82.
37. Reference deleted in proof.
38. Becker, R., M. Braack, …, B. Vexler. 2013. Gascoigne 3D—a finite element toolbox (http://www.gascoigne.uni-hd.de).
39. Zimmerberg, J., and M. M. Kozlov. 2006. How proteins produce cellular membrane curvature. *Nat. Rev. Mol. Cell Biol.* 7:9–19.
40. Kralj-Iglic, V., V. Heinrich, …, B. Zeks. 1999. Free energy of closed membrane with anisotropic inclusions. *Eur. Phys. J. B.* 10:5–8.

41. Fosnaric, M., K. Bohinc, …, S. May. 2005. The influence of anisotropic membrane inclusions on curvature elastic properties of lipid membranes. *J. Chem. Inf. Model.* 45:1652–1661.

42. Iglic, A., B. Babnik, …, V. Kralj-Iglic. 2007. On the role of anisotropy of membrane constituents in formation of a membrane neck during budding of a multicomponent membrane. *J. Biomech.* 40:579–585.

43. Chen, C. M. 2000. Theory for the bending rigidity of protein-coated lipid membranes. *Physica A.* 281:41–50.

44. Pott, T., C. Gerbeaud, …, P. Méléard. 2015. Melittin modifies bending elasticity in an unexpected way. *Chem. Phys. Lipids.* 185:99–108.

45. Settles, E. I., A. F. Loftus, …, R. Parthasarathy. 2010. The vesicle trafficking protein Sar1 lowers lipid membrane rigidity. *Biophys. J.* 99:1539–1545.

46. Loftus, A. F., S. Noreng, …, R. Parthasarathy. 2013. Robust measurement of membrane bending moduli using light sheet fluorescence imaging of vesicle fluctuations. *Langmuir.* 29:14588–14594.

47. Hu, M., J. J. Briguglio, and M. Deserno. 2012. Determining the Gaussian curvature modulus of lipid membranes in simulations. *Biophys. J.* 102:1403–1410.

48. Jung, H.-T., S. Y. Lee, …, J. A. Zasadzinski. 2002. Gaussian curvature and the equilibrium among bilayer cylinders, spheres, and discs. *Proc. Natl. Acad. Sci. USA.* 99:15318–15322.

49. Allain, J.-M., C. Storm, …, J.-F. Joanny. 2004. Fission of a multiphase membrane tube. *Phys. Rev. Lett.* 93:158104.

50. Baumgart, T., S. T. Hess, and W. W. Webb. 2003. Imaging coexisting fluid domains in biomembrane models coupling curvature and line tension. *Nature.* 425:821–824.

51. Ramadurai, S., R. Duurkens, …, B. Poolman. 2010. Lateral diffusion of membrane proteins: consequences of hydrophobic mismatch and lipid composition. *Biophys. J.* 99:1482–1489.

52. Murk, J. L. A. N., B. M. Humbel, …, M. J. Kleijmeer. 2003. Endosomal compartmentalization in three dimensions: implications for membrane fusion. *Proc. Natl. Acad. Sci. USA.* 100:13332–13337.

53. Wilhelm, C., A. Cebers, …, F. Gazeau. 2003. Deformation of intracellular endosomes under a magnetic field. *Eur. Biophys. J.* 32:655–660.

54. Gracià, R., N. Bezlyepkina, …, R. Dimova. 2010. Effect of cholesterol on the rigidity of saturated and unsaturated membranes: fluctuation and electrodeformation analysis of giant vesicles. *Soft Matter.* 6:1472–1482.

55. Reference deleted in proof.

56. Reference deleted in proof.

57. Reference deleted in proof.

58. Lipowsky, R. 2013. Spontaneous tubulation of membranes and vesicles reveals membrane tension generated by spontaneous curvature. *Faraday Discuss.* 161:305–331, discussion 419–459.

59. Lipowsky, L. 1992. Budding of membranes induced by intramembrane domains. *J. Phys. II France.* 2:1825–1840.

60. Pearse, B. M. 1976. Clathrin: a unique protein associated with intracellular transfer of membrane by coated vesicles. *Proc. Natl. Acad. Sci. USA.* 73:1255–1259.

61. Mashl, R. J., and R. F. Bruinsma. 1998. Spontaneous-curvature theory of clathrin-coated membranes. *Biophys. J.* 74:2862–2875.

62. Schmidt, U., G. Guigas, and M. Weiss. 2008. Cluster formation of transmembrane proteins due to hydrophobic mismatching. *Phys. Rev. Lett.* 101:128104.

63. Blanchette, C. D., W.-C. Lin, …, M. L. Longo. 2008. Domain nucleation rates and interfacial line tensions in supported bilayers of ternary mixtures containing galactosylceramide. *Biophys. J.* 94:2691–2697.

64. Parthasarathy, R., C. H. Yu, and J. T. Groves. 2006. Curvature-modulated phase separation in lipid bilayer membranes. *Langmuir.* 22:5095–5099.

65. Wang, H., D. Hu, and P. Zhang. 2013. Measuring the spontaneous curvature of bilayer membranes by molecular dynamics simulations. *Commun. Comput. Phys.* 13:1093–1106.

66. Yin, Y., J. Yin, and J. Wu. 2007. The second gradient operator and integral theorems for tensor fields on curved surfaces. *Appl. Math. Sci.* 1:1465–1484.

67. Ni, D., Y. Yin, and H. Shi. 2005. Equilibrium shape equation and geometrically permissible condition for two-component lipid bilayer vesicles. *J. Biol. Phys.* 31:135–143.

68. Zhong-Can, O., and W. Helfrich. 1989. Bending energy of vesicle membranes: general expressions for the first, second, and third variation of the shape energy and applications to spheres and cylinders. *Phys. Rev. A.* 39:5280–5288.

69. Das, S., J. Jenkins, and T. Baumgart. 2009. Neck geometry and shape transitions in vesicles with co-existing fluid phases: role of Gaussian curvature stiffness vs. spontaneous curvature. *Europhys. Lett.* 86:1–6.

70. Jülicher, F., and R. Lipowsky. 1996. Shape transformations of vesicles with intramembrane domains. *Phys. Rev. E Stat. Phys. Plasmas Fluids Relat. Interdiscip. Topics.* 53:2670–2683.

71. Kwak, D. 2008. The sharp-interface limit of the Cahn-Hilliard system with elasticity. PhD thesis, Regensburg University, Regensburg, Germany.

72. Elliott, C. M., and B. Stinner. 2010. A surface phase field model for two-phase biological membranes. *SIAM J. Appl. Math.* 70:2904–2928.

73. Kondo, S., and T. Miura. 2010. Reaction-diffusion model as a framework for understanding biological pattern formation. *Science.* 329:1616–1620.

74. Murray, J. 2003. Mathematical Biology II: Spatial Models and Biomedical Applications. Springer-Verlag, Berlin, Heidelberg.

75. Goryachev, A. B., and A. V. Pokhilko. 2008. Dynamics of Cdc42 network embodies a Turing-type mechanism of yeast cell polarity. *FEBS Lett.* 582:1437–1443.

76. Orlandini, E., D. Marenduzzo, and A. Goryachev. 2013. Domain formation on curved membranes: phase separation or Turing patterns? *Soft Matter.* 9:9311–9318.

77. Campelo, F., H. T. McMahon, and M. M. Kozlov. 2008. The hydrophobic insertion mechanism of membrane curvature generation by proteins. *Biophys. J.* 95:2325–2339.

78. Ryu, Y.-S., I.-H. Lee, …, S.-D. Lee. 2014. Reconstituting ring-rafts in bud-mimicking topography of model membranes. *Nat. Commun.* 5:4507.